Energy & Environmental Science

ROYAL SOCIETY OF CHEMISTRY

PAPER

View Article Online
View Journal | View Issue

Cite this: *Energy Environ. Sci.*, 2025, **18**, 439

23.2% efficient low band gap perovskite solar cells with cyanogen management†

W. Hashini K. Perera, ‡[a] Thomas Webb, ‡[b] Yuliang Xu, [c] Jingwei Zhu, [c] Yundong Zhou, [d] Gustavo F. Trindade, [d] Mateus G. Masteghin, [a] Steven P. Harvey, [e] Sandra Jenatsch, [f] Linjie Dai, [gh] Sanjayan Sathasivam, [ij] Thomas J. Macdonald, [k] Steven J. Hinder, [l] Yunlong Zhao, [dm] Samuel D. Stranks, [gh] Dewei Zhao, [c] Wei Zhang, [a] K. D. G. Imalka Jayawardena, *[a] Saif A. Haque *[b] and S. Ravi P. Silva *[a]

Received 8th July 2024,
Accepted 11th November 2024

DOI: 10.1039/d4ee03001j

rsc.li/ees

Managing iodine formation is crucial for realising efficient and stable perovskite photovoltaics. Poly(3,4-ethylenedioxythiophene)polystyrene sulfonate (PEDOT:PSS) is a widely adopted hole transport material, particularly for perovskite solar cells (PSCs). However, improving the performance and stability of PEDOT:PSS based perovskite optoelectronics remains a key challenge. We show that amine-containing organic cations de-dope PEDOT:PSS, causing performance loss, which is partially recovered with thiocyanate additives. However, this comes at the expense of device stability due to cyanogen formation from thiocyanate–iodine interaction which is accelerated in the presence of moisture. To mitigate this degradation pathway, we incorporate an iodine reductant in lead–tin PSCs. The resulting devices show an improved power conversion efficiency of 23.2% which is among the highest reported for lead–tin PSCs, and ~66% enhancement in the T_{S80} lifetime under maximum power point tracking and ambient conditions. These findings offer insights for designing next-generation hole extraction materials for more efficient and stable PSCs.

Broader context

Poly(3,4-ethylenedioxythiophene)polystyrene sulfonate (PEDOT:PSS) is the hole extracting polymer of choice for tin-based perovskite solar cells, including narrow bandgap lead–tin perovskites which are used in high efficiency all-perovskite multijunction solar cells. However, using PEDOT:PSS results in both efficiency losses and device instability. Additives such as thiocyanates are routinely incorporated into perovskite absorbers for devices that use PEDOT:PSS as the hole transport layer. While this improves the device stability under inert conditions, these devices are still susceptible to degradation under ambient conditions. In this study, we identify the origin of the performance losses for perovskite solar cells fabricated on PEDOT:PSS, and the mechanism by which thiocyanates mitigate these losses while improving device stability under inert conditions. We further demonstrate that in the presence of moisture, thiocyanates form cyanogens which accelerate the perovskite degradation, irrespective of the hole transport layer used. Based on the above, we identify iodine reduction within the bulk as a key strategy to improve device efficiency as well as stability for lead–tin perovskites, when operated under ambient conditions. Our work provides key insights for designing hole transport layers for more stable and efficient perovskite solar cells and optoelectronic devices.

[a] *Advanced Technology Institute, School of Computer Science and Electronic Engineering, University of Surrey, Guildford, Surrey GU2 7XH, UK. E-mail: i.jayawardena@surrey.ac.uk, s.silva@surrey.ac.uk*
[b] *Department of Chemistry and Centre for Processable Electronics, Imperial College London, London W12 0BZ, UK. E-mail: s.a.haque@imperial.ac.uk*
[c] *College of Materials Science and Engineering and Engineering Research Centre of Alternative Energy Materials and Devices, Ministry of Education, Sichuan University, Chengdu 610065, China*
[d] *National Physical Laboratory, NiCE-MSI, Teddington TW11 0LW, UK*
[e] *Materials Science Centre, National Renewable Energy Laboratory, Golden, Colorado 80401, USA*
[f] *Fluxim AG, Katharina-Sulzer-Platz 2, 8406 Winterthur, Switzerland*
[g] *Department of Chemical Engineering and Biotechnology, University of Cambridge, Cambridge CB3 0AS, UK*
[h] *Department of Physics, Cavendish Laboratory, University of Cambridge, Cambridge CB3 0HE, UK*
[i] *School of Engineering, London South Bank University, London SE1 0AA, UK*
[j] *Department of Chemistry, University College London, 20 Gordon Street, London WC1H 0AJ, UK*
[k] *Department of Electronic & Electrical Engineering, University College London, London WC1E 7JE, UK*
[l] *The Surface Analysis Laboratory, Faculty of Engineering and Physical Sciences, University of Surrey, Guildford, Surrey GU2 7XH, UK*
[m] *Dyson School of Design Engineering, Imperial College London, London SW7 2BX, UK*

† Electronic supplementary information (ESI) available. See DOI: https://doi.org/10.1039/d4ee03001j

‡ These authors contributed equally.

Introduction

Efficiency, stability, and scalability – all while being cost effective – remain the major challenges for perovskite solar cell (PSC) technologies. Independently verified power conversion efficiencies (PCEs) of 26.7% and 23.6% have been reported for single junction devices based on lead (Pb)[1] and lead–tin (Pb–Sn)[2] compositions, respectively. The rapid development of Pb–Sn perovskite devices is particularly crucial towards realising all-perovskite multijunction cells, which have PCEs now exceeding 30%,[1] and are anticipated to compete with perovskite/silicon multijunction cells as a low-cost alternative.

In recent years, PSCs have also seen impressive progress in operational stability with reports of stability beyond 4500 hours for the regular architecture[3] and over 1000 hours for the inverted architecture.[4–6] The instability of PSCs is accelerated through iodine formation which occurs when the perovskite absorber is subjected to stressors such as light, heat and moisture.[4,7–9] Once formed, iodine rapidly degrades the perovskite absorber, transport layers, and metal electrodes[9] and thereby, device performance.[10–12] Therefore, further advances in PCE and long-term operational stability will ultimately depend on the ability to identify and mitigate iodine-induced degradation pathways in PSCs.

For inverted PSCs, the buried interface plays a crucial role in device stability.[10,11,13] Poly(3,4-ethylenedioxythiophene)polystyrene sulfonate (PEDOT:PSS) is a flexible, water-based hole transport layer (HTL) used in a range of applications including light-emitting diodes (LEDs), biosensors, thermoelectrics and organic solar cells.[12] Its low cost[14] makes PEDOT:PSS a promising candidate for upscaling of PSCs for manufacturing. PEDOT:PSS also exhibits good charge transport at film thicknesses >30 nm, ensuring better tolerance to large-area manufacturing by reducing pinhole formation, a challenge faced with thin organic HTLs and self-assembled monolayers (SAMs).[14–17] PEDOT:PSS has also been the HTL of choice for single junction Sn[18,19] and Pb–Sn[2,20] PSCs, as well as in multijunction tandem devices with Pb–Sn sub-cells,[21–23] mainly due to its favourable energy level alignment that allows efficient hole extraction.[24]

PEDOT:PSS comprises two coulombically bound ionomers which offer unique challenges concerning performance and stability. The dependence of the conducting poly(3,4-ethylenedioxythiophene) (PEDOT) polymer upon polystyrene sulfonate (PSS) for both stabilisation of charge and aqueous solubility strongly influences the doping and morphology characteristics and thereby its electronic properties.[25] Consequently, PEDOT:PSS films are highly sensitive to factors such as pH, processing parameters, and undesirable de-doping. To this end, significant PCE and stability losses have been observed when PEDOT:PSS is used in PSCs based on Pb, Pb–Sn and Sn compositions compared to other HTLs,[26–28] whose origins are yet to be fully understood.

Thiocyanate (SCN^-) salts are some of the most widely used additives in single and multijunction PSCs in both wide bandgap Pb, and Pb–Sn absorbers.[29–33] However, the mechanism(s) by which SCN^- improves the performance of PSCs is/are still a topic of debate. An increase in perovskite grain size has been near-universally reported within the literature upon the direct addition of SCN^- salts to the precursor,[34] while other studies have also suggested incorporation within the perovskite lattice, phase stabilisation, and complexation with the metal centre as well as a reduction of the trap density at the buried interface between PEDOT:PSS and the perovskite.[35,36] While PSCs incorporating SCN^- have been reported to result in improved device stability, a majority of these have focused on the stability of devices in an inert environment (Table S1, ESI†) with devices tested under ambient and high humidity conditions showing poor stability relative to other HTLs.[37] Therefore, understanding the origin and mechanism of this instability will be a key step towards the commercialisation of perovskite photovoltaics based on PEDOT:PSS.[38]

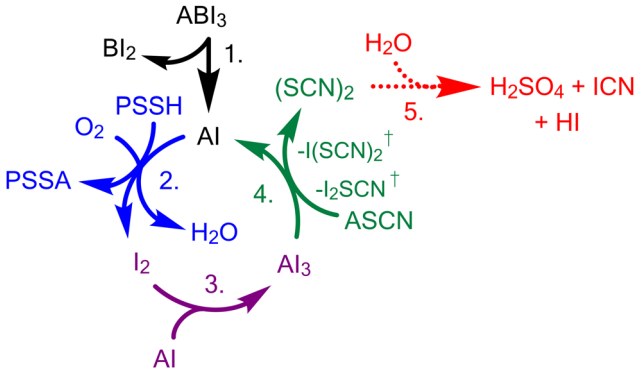

Fig. 1 Reaction scheme for the interfacial chemistry occurring between PEDOT:PSS and perovskite. A denotes an organic cation, B a metal cation, I is iodine, and PSS is polystyrene sulfonate anion. Reaction (1): breakdown of the ABI_3 perovskite lattice into its constituent salts (BI_2, AI). Reaction (2): oxidation of iodides (I^-) and reduction of $PEDOT^{n+}$ at the PEDOT:PSS *via* the formation of an organic cation-polystyrene sulfonate salt (PSSA or A:PSS). Reaction (3): reaction of I_2 within the perovskite to form corrosive triiodide (I_3^-) species, AI_3. Reaction (4): reduction of I_3^- with thiocyanate (SCN^-) salts *via* iodo-thiocyanate intermediates, reforming the organohalide and unstable thiocyanogen species. Reaction (5): hydrolysation of $(SCN)_2$ thiocyanogen into iodine cyanide (ICN), sulphuric acid (H_2SO_4) and hydroiodic acid (HI).

In this work, we employ a combination of chemical, electronic and computational methods, to identify the origin of the poor performance and stability of PSCs utilising PEDOT:PSS as the HTL and the important role of SCN^- additives in the performance and stability in these devices. We show that de-doping of PEDOT:PSS originates from the diffusion of amines from the perovskite photoactive layer (Fig. 1: reactions (1) and (2)). This results in the generation of highly corrosive iodine species and triiodide (I_3^-) species which subsequently facilitates the degradation of device performance and stability (Fig. 1: reaction (3)). We show that the incorporation of amine-containing thiocyanates significantly impedes this diffusion process, thereby reducing the extent of de-doping at the PEDOT:PSS interface, and effectively scavenges any corrosive iodine species (Fig. 1: reaction (4)). This results in a ~30% performance improvement in Pb and Pb–Sn PSCs. However, under high humidity conditions relevant to ISOS test protocols (relative humidity, RH = 65%), we identify that the thiocyanogen by-products of the neutralisation of molecular

iodine (I_2) with SCN^- are highly susceptible to hydrolysation, forming corrosive cyanogens (Fig. 1: reaction (5)). These compounds can readily compromise the ambient stability of the SCN^- containing devices, particularly those susceptible to I_2 formation, contributing to the short device lifetimes typically observed in Sn and Pb–Sn PSCs.[2,29,30] By adding benzyl hydrazine chloride (BHC), an iodine reductant,[31] we demonstrate a champion PCE of 23.2%. Specifically, the use of BHC introduces a new chemical pathway that successfully competes with reaction (4) (Fig. 1) and minimises cyanogen formation. Furthermore, these BHC incorporated devices show a ~66% improvement in the T_{S80} lifetime under maximum power point tracking (MPPT) and ambient conditions compared to devices without BHC. Our findings offer new chemical insights for the rational design of next-generation hole extraction materials and iodine management strategies to enhance efficiency and stability in PSCs.

Results and discussion

Effect of PEDOT:PSS and thiocyanate additives on device performance and stability

To evaluate the influence of the buried interface on device performance, we fabricated and tested devices with a methylammonium lead iodide (MAPI) absorber layer based on the inverted p–i–n architecture (Fig. 2a and b) consisting of indium tin oxide (ITO)/poly(triarylamine) (PTAA)/MAPI/C_{60}/bathocuproine (BCP)/silver (Ag) (reference) and ITO/PEDOT:PSS/MAPI/C_{60}/BCP/Ag. MAPI was chosen to circumvent complications such as compositional variation, phase segregation and the instability of Sn precursors.[22,30,32]

The current density *vs.* voltage (*J–V*) characteristics of the champion device based on PEDOT:PSS (Fig. 2c) shows significant losses in open circuit voltage (V_{OC}) and short circuit current density (J_{SC}). For devices based on PTAA, we achieved a champion PCE of ~19%, while the champion PEDOT:PSS device showed a lower PCE of 11.4%. The external quantum efficiency (EQE) spectra (Fig. 2d), also show a notable loss in photocurrent throughout the absorption range for the PEDOT:PSS device. This is indicative of higher recombination within the bulk absorber and/or poor charge extraction. With the addition of thiocyanates (lead thiocyanate ($Pb(SCN)_2$) or guanidinium thiocyanate (GASCN)), we observed a significant PCE enhancement driven by improvements across all device parameters in PEDOT:PSS devices under optimised concentrations of the additives (Fig. 2c, d and Fig. S1–S3, ESI†). Furthermore, a difference in J_{SC} was observed between the solar simulator and EQE measurements for devices based on PEDOT:PSS, which is reduced upon the incorporation of SCN^-. We attribute this to the more dominant ion migration in these devices, which particularly influences the J_{SC} values based on measurements that require longer durations such as EQE measurement. In comparison, this current mismatch is less evident for PTAA based devices where ion migration effects are weaker, as discussed later. We further note that the improvements in device performance following the addition of SCN^- discussed above for MAPI was also observed for Pb–Sn perovskites (Fig. S4, ESI†).

To identify the origin of the observed device losses, we carried out time and frequency domain characterisation of the device stacks. Using transient absorption spectroscopy (TAS), we obtained a Shockley–Read–Hall (SRH) recombination rate constant (k_1) of 1.22×10^6 s^{-1} for PEDOT:PSS/MAPI followed by a slower rate constant of 5.40×10^5 s^{-1} for PEDOT:PSS/MAPI+SCN^- with PTAA/MAPI showing the smallest rate constant of 1.05×10^5 s^{-1} (Fig. S5 and Note S1, ESI†). The smaller k_1 for PEDOT:PSS/MAPI+SCN^- as compared to PEDOT:PSS/MAPI indicates a reduction in the trap density upon the addition of SCN^-. These results are further verified through transient photocurrent measurements (TPC, Fig. S6 and Note S2, ESI†). Additionally, in intensity modulated photocurrent spectroscopy (IMPS) characterisation, we observe a low-frequency peak (*i.e.* <100 Hz) for perovskite devices prepared on PEDOT:PSS, characteristic of increased ion migration.[33] These results point towards the buried PEDOT:PSS interface being a direct contributor to the observed performance losses.

We next studied the stability of these devices under ISOS-D-1 (dark, 65% RH) and ISOS-D-1I (dark, N_2 environment) test conditions.[39] Under ISOS-D-1 conditions (Fig. 2e and Fig. S7, S8, ESI†), the PEDOT:PSS devices showed a relative increase of ~20% in the PCE while an onset of degradation was observed for the PTAA devices. However, the PEDOT:PSS devices containing SCN^- showed an accelerated degradation with a T_{80} lifetime of ~250 h, significantly shorter than that of other device architectures investigated here. Along with changes in the PCE, we also observed changes in the perovskite microstructure (Fig. S9 and S10, ESI†). X-ray photoelectron spectroscopy (XPS) characterisation of half cells degraded under similar conditions indicated the presence of metallic Pb (Pb^0) on fresh perovskites formed on PEDOT:PSS in the absence of SCN^- (Fig. S11 and S12, ESI†), indicating the loss of iodide (I^-) from the absorber. In comparison, all three device architectures tested under ISOS-D-1I conditions demonstrated significantly improved stability over the same testing period (Fig. 2f). To assess whether the ISOS-D-1 humidity-driven instability of devices containing SCN^- is universal to other HTLs, we fabricated and tested the stability of MAPI+SCN^- devices based on PTAA and Me-4PACz modified with PFN–Br and alumina nanoparticles.[15] PTAA and Me-4PACz are generally regarded as more stable compared to PEDOT:PSS. However, we observed a rapid degradation of these devices (Fig. S13 and S14, ESI†), emphasising the key role of SCN^- additives in driving device degradation. The faster degradation observed for PTAA and Me-4PACz based PSCs compared to PEDOT:PSS based devices points towards the importance of additional factors such as the thickness and chemical functionality of the HTL in minimising degradation in SCN^- containing PSCs.

Chemistry at the buried interface

So far, we have shown that: (i) PEDOT:PSS/MAPI based solar cells exhibit relatively poor PCEs as compared to devices based on other HTLs such as PTAA; (ii) addition of SCN^- salts to the MAPI active layer significantly improves the PCE of PEDOT:PSS

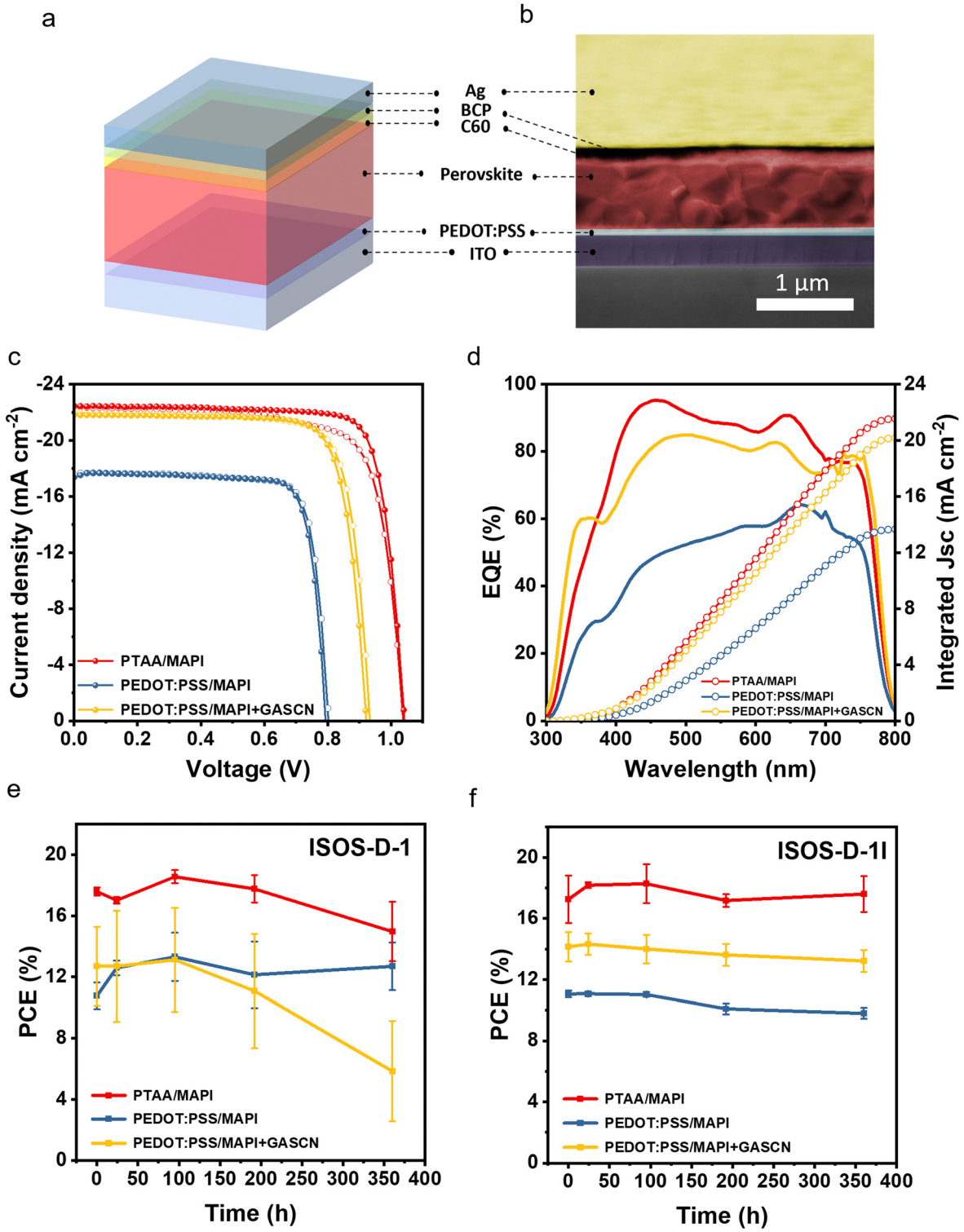

Fig. 2 Photovoltaic device performance and stability. (a) Device architecture of the PSCs. (b) A cross-sectional scanning electron microscope (SEM) image of the device, acquired at a 45° tilt. (c) *J*–*V* curves of the champion devices fabricated on PTAA and PEDOT:PSS with and without GASCN in MAPI under AM 1.5G illumination. (d) Corresponding external quantum efficiency (EQE) spectra and integrated photocurrent densities (J_{EQE}). (e) and (f) Stability testing of devices under (e) ISOS-D-1 (65% RH) and (f) ISOS-D-1I (N_2) conditions.

based devices and (iii) the improvement in PCE as reported in (ii) comes at the expense of stability upon exposure to a humid environment.

To understand the origin of these observations, we first studied the changes to the oxidation state of PEDOT:PSS using UV-visible absorbance spectroscopy (Fig. S15, ESI†), where an

increasing absorbance in the near IR region (NIR, >1100 nm) corresponds to a greater degree of oxidation.[27,40,41] With the addition of methylammonium iodide (MAI) to PEDOT:PSS, we observed a decrease in absorbance in the NIR range and an increase at 850 nm (Fig. 3a), where the latter absorbance peak is associated with the de-doped form of PEDOT:PSS (Fig. S16, ESI†).[40] This is further confirmed by electron paramagnetic resonance (EPR) measurements which showed a decrease in the integrated spin signal intensity, resembling sodium hydroxide (NaOH) induced de-doping (Fig. S17, ESI†).

To identify the origin of the observed PEDOT de-doping, we evaluated changes to the absorbance spectra of PSS with the

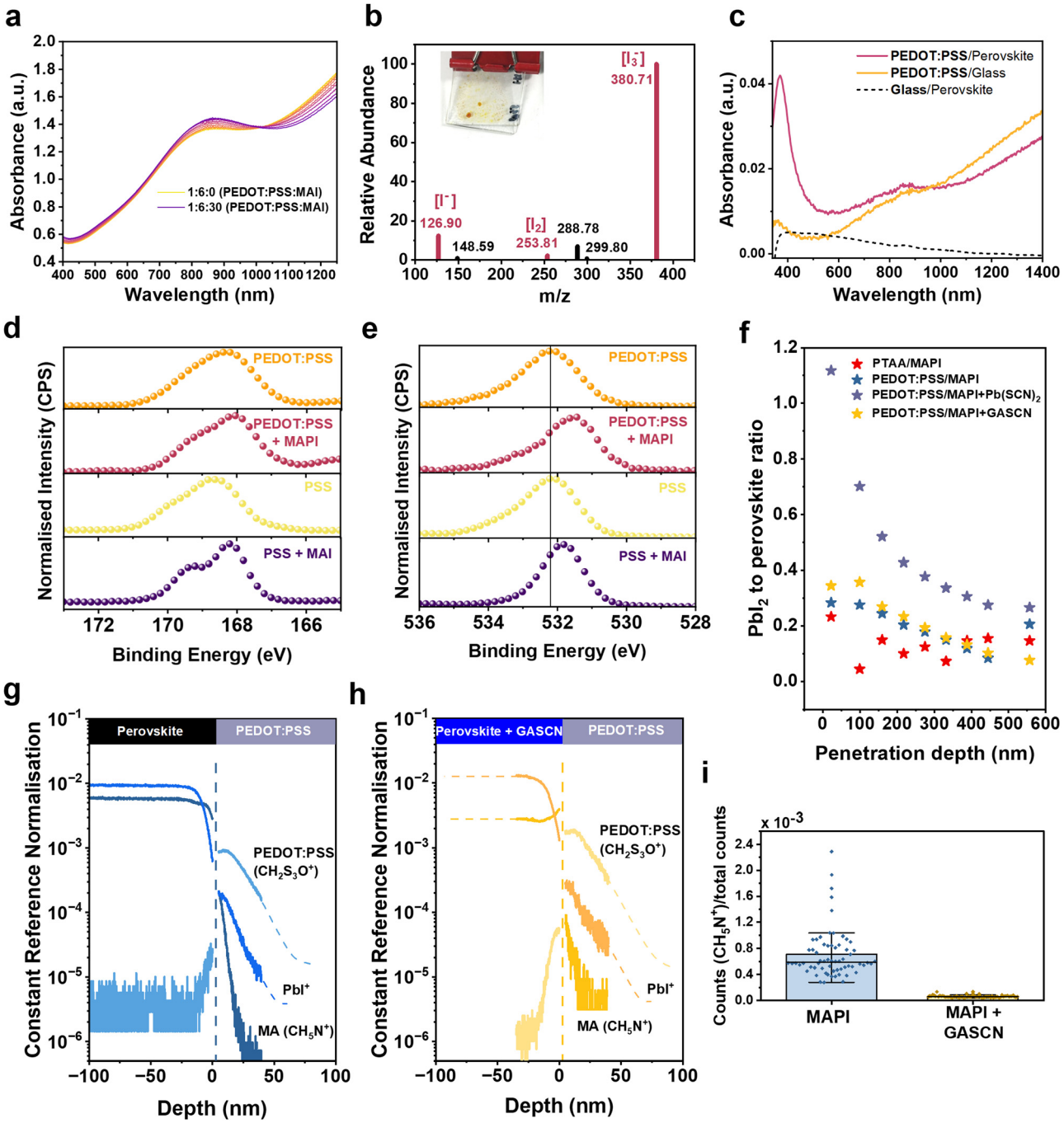

Fig. 3 Mechanism of de-doping and performance loss at the PEDOT:PSS/perovskite interface. (a) Absorbance spectra of the PEDOT:PSS solution with increasing concentrations of methylammonium iodide (MAI). (b) Mass spectra collected for the PSS solution combined with MAI revealing high concentrations of I_3^-, (inset) photograph of PSS coated glass pressed against MAI coated glass. (c) Comparison of the absorbance spectra of PEDOT:PSS films pressed against glass (yellow) or MAPI (pink). (d) and (e) X-ray photoelectron spectroscopy (XPS) of the (d) S 2p and (e) O 1s atomic orbitals. (f) Peak intensity ratios of PbI_2 to perovskite (110) as a function of penetration depth calculated from GIXRD data for grazing angles ranging from 0.25° to 2.5°. (g)–(i) Normalised ToF-SIMS depth profiles of (g) PEDOT:PSS/MAPI, (h) PEDOT:PSS/MAPI + GASCN and (i) total intensity analysis of $CH_3NH_2^+$ in PEDOT:PSS with and without GASCN.

MAI, where we observed the emergence of a new absorbance feature at 366 nm (Fig. S18, ESI†). Mass spectrometry (MS) of the solution (Fig. 3b)[27] identifies the newly formed species as I_3^- which was further confirmed upon comparison of reference absorbance spectra (Fig. S18, ESI†). These findings suggest that the mechanism of PEDOT de-doping by the organohalide proceeds *via* the deactivation of PSS, similar to NaOH induced de-doping (Fig. S19, ESI†).[27,28]

To demonstrate that the I_3^- is formed from the interaction between PSS and the organohalide within a solid-state interface, substrates coated with MAI and PSS films were pressed together and pressure applied (Fig. S20, ESI†). Within hours, the films stored under ambient conditions took a yellow appearance consistent with the formation of I_3^-, and confirmed *via* absorbance spectroscopy. Interestingly, under inert (N_2) conditions, significantly less I_3^- is detected, indicating that (i) oxygen is needed for the oxidation of I^- and (ii) sufficient oxygen remains trapped or electrocatalytically bound to the surface to drive the mechanism even within an inert atmosphere.[42] Replacing the PSS with PEDOT:PSS also facilitated the formation of I_3^- along with de-doping of the PEDOT:PSS (Fig. S20, ESI†), thus highlighting the role of the organohalide on PEDOT:PSS at the solid-state interface. Similarly, the formation of I_3^- and de-doping of the PEDOT:PSS was also observed in a solid-state PEDOT:PSS/MAPI interface (Fig. 3c and Fig. S20, ESI†).

To further study the nature of the interaction between PSS and the organohalide at the interface of PEDOT:PSS/MAPI, we combined XPS with sputtering. For this, MAPI was spin coated on PEDOT:PSS (sample 1) and compared with a model PSS/MAI interface (sample 2) prepared by pressing together films as discussed previously. In sample 1, we observed a decrease in the binding energies of S 2p and O 1s orbitals, attributed to the sulfonate group ($-SO_3^-$) of PSS, relative to that of pristine PEDOT:PSS. An identical decrease in the electron binding energies of S 2p and O 1s orbitals was observed in the spectra of sample 2 (Fig. 3d and e), further demonstrating the interaction between PSS and MAI as the origin of the chemical modification of PEDOT:PSS when applied in PSCs. Interestingly, while a similar decrease in the binding energies was observed for the $-SO_3^-$ group upon exposure of PSS to NaOH (Fig. S21, ESI†), no shift was present upon the addition of hydroiodic acid (HI), highlighting the importance of the cation and suggesting the formation of PSS-organic cation salt.

To obtain further evidence for the interaction between PEDOT:PSS and the perovskite, grazing incidence X-ray diffraction (GIXRD) was used to probe relative changes in the lead iodide (PbI_2) content as a function of the perovskite absorber depth. For PEDOT:PSS/MAPI we observed a notable increase in PbI_2 closer to the buried interface (Fig. 3f and Fig. S22, ESI†), consistent with the diffusion of methylammonium cations (MA^+) near the buried interface into PEDOT:PSS. This agrees with the chemical insights discussed above. The formation of a localised organic cation-poor region around the interface was not observed for MAPI deposited on PTAA. This highlights the importance of PEDOT:PSS in enabling this change in composition. Moreover, the PbI_2 excess (organohalide deficiency) near the buried interface was reduced upon inclusion of GASCN, which also showed a more homogenous distribution of PbI_2 through the film thickness, a feature also evident from time-of-flight secondary ion mass-spectrometric (ToF-SIMS) measurements (Fig. S23, ESI†). A similar trend was observed for $Pb(SCN)_2$. To verify the diffusion of MA^+ into PEDOT:PSS, we carried out ToF-SIMS on PEDOT:PSS exposed by cleavage of PEDOT:PSS/MAPI samples prepared with or without SCN^- salts (see the Methods section for details on sample preparation). In agreement with previous results, the ToF-SIMS measurements show the tendency of MA^+ to diffuse into PEDOT:PSS in samples prepared with MAPI (Fig. 3g), which is reduced upon the addition of GASCN (Fig. 3g–i and Fig. S24, ESI†).

Having shown that the MAI salt in the perovskite reacts with PSS, thereby de-doping the HTL and generating I_2 (Fig. 1 and eqn (1)), we next demonstrate that this mechanism is ubiquitous amongst other organohalides (Fig. S25, ESI†). As before, using absorbance spectroscopy, we compared the changes in the absorbance intensity of PEDOT:PSS at 1200 nm and 866 nm (corresponding to its higher and lower oxidation states respectively) upon the addition of MAI, formamidinium iodide (FAI) and guanidinium iodide (GAI). From Fig. 4a and b, it is evident that increasing the number of amine groups on the organohalide leads to increased de-doping of PEDOT:PSS, which is further supported by EPR spectroscopy (Fig. S26, ESI†). We also observed aggregation of PEDOT in PEDOT:PSS films following the deactivation of PSS with the organohalide (Fig. S27–S33, ESI†), a consequence of the organohalides blocking PSS's role in producing micelles around PEDOT during deposition. Furthermore, we find that both the degree of aggregation and de-doping ability increases with increasing amine groups ($MA^+ < FA^+ < GA^+$).

$$4PSSH + 4AI + O_2 \rightarrow 4PSS^-A^+ + 2H_2O + 2I_2 \qquad (1)$$

We employed density functional theory (DFT) to investigate the thermodynamics of eqn (1) and the associated ionic binding energies of the salts involved. DFT predicts a favourable thermodynamic driving force (ΔG_r) for the forward reaction, eqn (1), for all three cations investigated (Fig. 4c). Next, we evaluated the ionic binding energy ΔG_b(A:PSS) between the PSS anion and organic cation A^+. As expected, increasing the delocalisation of the cation across multiple amine groups decreased the strength of the ionic binding energy with the PSS anion (Fig. S34, ESI†).[43–45] This is further confirmed in the electronic surface potential (ESP) maps of the PSS:A salts following structural optimisation (Fig. 4d–g) and by consideration of the total Mullikan charge across the PSS sulfonate anion ($-SO_3^-$) (Fig. S35, ESI†). Using XPS to compare the electron density on the S 2p orbital of the PSS sulfonate group in the absence and presence of the organohalide, we observed an increase in the electron density on $-SO_3^-$ upon exposure to MAI which is further increased upon exposure to FAI (Fig. S36, ESI†). We calculated the displacement energy ΔG_d(PEDOT/A:PSS), defined as the difference in free energy for an isolated A^+ cation to displace a PEDOT trimer, forming a highly ionic A:PSS salt and isolated PEDOT cations (see the methods

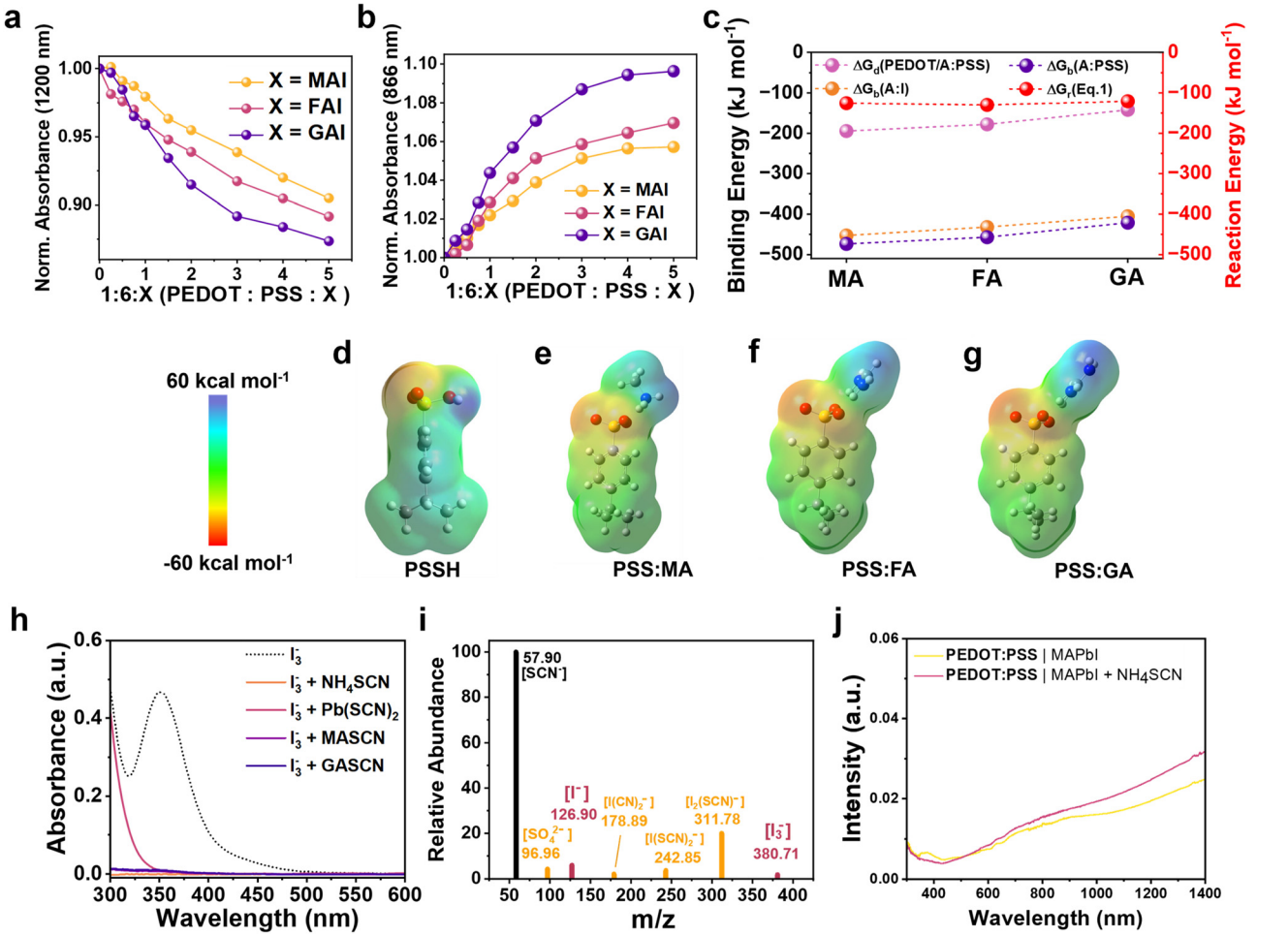

Fig. 4 The effect of cation choice on PEDOT:PSS de-doping. (a) and (b) Absorbance spectra of PEDOT:PSS with various A site cations of the (a) high oxidation state (1200 nm) and (b) lower oxidation state (866 nm). (c) Density functional theory (DFT) predictions of the displacement energy between PEDOT:PSS and A:PSS (PEDOT/A:PSS), ionic binding energy of the AI salt (A:I), ionic binding energy of the A:PSS salt (A:PSS), and reaction energy of eqn (1), calculated using a 6-311G(d,p) (H,C,N,O,S) + LANL2DZ (I) hybrid basis set (see the methods section). (d)–(g) Electronic surface potential of a PSS-cation ionic pair when interacting with (d) H^+, (e) MA^+, (f) FA^+, and (g) GA^+. (h) Absorbance spectra showing neutralisation of a MAI_3 reference solution following the addition of various SCN^- salts. (i) Mass spectra of the MAI_3 solution following the addition of ammonium thiocyanate (NH_4SCN). (j) Absorbance spectra of the PEDOT:PSS films following pressing against MAPI perovskite films with and without NH_4SCN under a N_2 atmosphere for 7 days.

Table 1 Gas-phase DFT calculations for reaction, ionic binding and displacement energies (kJ mol^{-1})

Organic cation	ΔG_r (eqn (1))	ΔG_b(A:PSS)	ΔG_d(PEDOT/A:PSS)
MA^+	−125.4	−473.6	−194.5
FA^+	−129.6	−457.0	−177.9
GA^+	−120.6	−421.1	−142.0

section). The ΔG_d(PEDOT/A:PSS) values for MA^+, FA^+ and GA^+ (Table 1) indicate the capability of these cations to displace and destabilise PEDOT in PEDOT:PSS, in agreement with the experimentally observed de-doping at the perovskite/PEDOT:PSS interface.

When accounting for the factors which can dictate trends in de-doping, it is important to consider the binding energy ΔG_b(A:PSS) of the organohalide salts (Table 1). In this case, the increased delocalisation of the charge reduces the ionic binding energy with the halide. This allows for the oxidation of the I^- anions which generates free organic cations to form a salt and deactivate the PSS (eqn (1)). Additionally, we note that the charge delocalisation across multiple amine groups increases ΔG_b(A:PSS) when a second neighbouring PSS group is introduced. In this case, the delocalisation of the charge enables bridging between the two SO_3^- groups thereby allowing a single organic cation to interact strongly with adjoining PSS monomers (Fig. S37, ESI†). As such, the local stoichiometry and concentration effects between the organic cations and PSS will likely influence the co-ordination to PSS and its subsequent deactivation. From this comparison, we hypothesise that the observed trend in de-doping ability, from a thermodynamic viewpoint, is driven by a combination of the stability of the

initial organohalide salt, the concentration of the organic cation available to displace PEDOT in PEDOT:PSS, and the binding strength of the PSS with the organic cation. However, additional factors such as the PSS micelle size, the inability of GA^+ to occupy a 3D perovskite lattice position, mobility/diffusion of the organic cation, and defect density will also have a role in dictating the de-doping of PEDOT:PSS.

So far, we have discussed the chemical reactions at the PEDOT:PSS/perovskite interface which are responsible for de-doping of the HTL and leading to the formation of I_3^-. We next investigated the role of SCN^- salts in mitigating this issue. We first directly added SCN^- salts to MAI_3 solutions and observed a colour change from yellow to colourless, consistent with the reduction of I_3^- to I^- (Fig. 4h and Fig. S38, ESI†). Notably, in the case of $Pb(SCN)_2$, the reaction with MAI_3 formed a bright yellow precipitate attributed to PbI_2 (Fig. S38, ESI†). Cyclic voltammetry (CV) was used to compare the redox potentials of I_2 and ammonium thiocyanate (NH_4SCN) using tetrabutylammonium hexafluorophosphate [nBu$_4$PF$_6$], an anhydrous and degassed acetonitrile electrolyte (Fig. S39, ESI†). The collected voltammograms revealed similar redox potentials between the SCN^- and I_2,[46–48] making the reaction susceptible to additional parameters including the concentrations of $[I^-]$:$[I_3^-]$:$[I_2]$ and most notably, the concentration of trace water (the importance of this is discussed shortly). Indeed, upon the addition of SCN^- ions to I_2 or *vice versa*, we observed the formation of a second redox peak consistent with the introduction of I^- into the equilibrium and subsequent formation of I_3^-. To further confirm the reduction of I_2, as well as to identify by-products, MS analysis was performed on MAI_3 following the addition of NH_4SCN (Fig. 4i). Two additional small peaks in the mass spectra with fragment masses of 242.85 a.u. and 311.78 a.u. are identified as $[I(SCN)_2]^-$ and $[I_2(SCN)]^-$ and correspond to the intermediates of I_2 reduction/SCN^- oxidation as given in eqn (2)–(4).[49]

$$I_2 + SCN^- \rightarrow I_2(SCN)^- \quad (2)$$

$$I_2(SCN)^- + 3SCN^- \rightarrow 2I(SCN)_2^- + 2e^- \quad (3)$$

$$I(SCN)_2^- \rightleftharpoons I^- + (SCN)_2 \quad (4)$$

Mass spectra also revealed additional peaks with masses of 96.96 a.u. and 178.88 a.u. corresponding to sulphate (SO_4^{2-}) and $[ICN(CN)]^-$, respectively. This is consistent with the hydrolysis of thiocyanogen $(SCN)_2$, the oxidation product of SCN^-. Under this mechanism, upon contact with ambient moisture, hygroscopic $(SCN)_2$ species undergo hydrolysation forming iodine cyanide (ICN), hydrogen cyanide (HCN) and sulphuric acid (H_2SO_4) as indicated in eqn (5)–(8) (Fig. 1: reaction (5)). Additional mass spectra were collected using anhydrous isopropyl alcohol dried over molecular sieves where identical hydrolysation products were recorded, demonstrating the high degree of moisture sensitivity of the reactions following the brief exposure to ambient conditions during sample loading (Fig. S40, ESI†).

$$I_3^- + 2e^- \rightarrow 3I^- \quad (5)$$

$$2SCN^- \rightarrow 2e^- + (NCS)_2 \quad (6)$$

$$3(SCN)_2 + 4H_2O \rightarrow H_2SO_4 + HCN + 5H^+ + 5SCN^- \quad (7)$$

$$8I_2 + 2SCN^- + 8H_2O \rightarrow 2H_2SO_4 + 2ICN + 14I^- + 12H^+ \quad (8)$$

A combination of ^{1}H and ^{13}C nuclear magnetic resonance (NMR) techniques (Fig. S41, ESI†) was employed to further study the nature of the decomposition products. Upon addition of I_2 to a suspension of $Pb(SCN)_2$ in chloroform-D ($CDCl_3$), we observed a downfield shift in the H_2O trace peak from 1.59 ppm to 1.62 ppm consistent with acidification and the formation of the hydronium ion (H_3O^+). Likewise, attenuated total reflection Fourier transform infrared (ATR-FTIR) spectroscopic measurements on NH_4SCN before and after I_2 exposure shows the formation of a new peak around 3500 cm^{-1}, consistent with H_2SO_4 evolution (Fig. S42, ESI†). ^{13}C NMR on the same $Pb(SCN)_2$ solution before and after the addition of I_2 (Fig. S41, ESI†) showed no clear peaks in the former owing to the insolubility of the SCN^- salt in the solvent. Upon addition of I_2 to the solution, we observed a new peak at 30.95 ppm, consistent with the formation of ICN. However, we note this peak was not observed when NMR samples were prepared using extra dry solvents and carefully desiccated inorganic salts whereby thiocyanogen compounds do not undergo hydrolysation and subsequent decomposition.

We next investigated the impact of ambient moisture in facilitating the reduction of I_3^- *via* oxidation and subsequent hydrolysation of SCN^- anions. To do this, changes in the CN bond were measured using ATR-FTIR following the reaction of NH_4SCN with MAI_3 in solid–liquid and solid–solid phases under ambient conditions (Fig. S43, ESI†). In each case, the C–N stretch of SCN was shifted to lower frequencies. These results are as expected owing to the highly hygroscopic nature of SCN^- salts. Similarly, confocal Raman spectroscopy probing NH_4SCN before and after mixing with solid MAI_3 revealed a shift and broadening of the low-frequency S–C bend, demonstrating the availability of sufficient ambient moisture for SCN^- to react with I_3^- (Fig. S44, ESI†).

We now consider the implications of this fundamental chemistry on device performance. The presence of I_3^- has previously been linked to the formation of shallow traps, while de-doping of PEDOT:PSS leads to reduced conductivity and the formation of a charge extraction barrier which degrades PSC performance (Fig. S45–S47, ESI†).[31,50,51] We attribute the improved device PCE in SCN^- containing devices to the neutralisation and the reduction of I_3^- traps. Indeed, PEDOT:PSS/MAPI interfaces prepared with NH_4SCN added to the perovskite precursor resulted in less I_3^- and reduced de-doping of the PEDOT:PSS, as compared to those without SCN^- (Fig. 4j and Fig. S48, ESI†). While the reduction in I_3^- is undoubtedly beneficial to the performance and longevity of the resulting cells, we note this stability improving mechanism (I_3^- scavenging *via* SCN^-, Fig. 1: reaction (4)) is likely to be offset by the rapid hydrolysation of the formed thiocyanogen (Fig. 1: reaction (5)), particularly under humid conditions or at high SCN^- loadings. Indeed, the corrosive nature of cyanogen and

iodocyanogens explains the poor stability of SCN^- containing devices under moisture or high RH conditions (Fig. 2e and f).

Effect of iodine reductant on the stability and efficiency in Pb–Sn cells

Next, we sought to investigate if the incorporation of an iodine reducing agent can improve the performance and stability of Pb–Sn mixed PSCs by switching off reaction (4) (Fig. 1). To this end, we incorporated BHC (Note S4, ESI†), an iodine reductant,[44] into the Pb–Sn precursor and fabricated devices with the architecture of glass/ITO/PEDOT:PSS/perovskite/C_{60}/BCP/copper (Cu). Examples for other reductants and scavengers are discussed in ref. 9 and exemplars are given in Table S2 (ESI†). The incorporation of BHC resulted in devices with a champion PCE of 23.18%, J_{SC} of 31.84 mA cm^{-2}, V_{OC} of 0.875 V and a fill factor (FF) of 83.23% (Fig. 5a, Table 2 and Fig. S49, ESI†). In comparison, the control device showed a lower PCE of 21.86%, with a J_{SC} of 31.53 mA cm^{-2}, V_{OC} of 0.852 V and FF of 81.41%. The enhancement in the FF particularly is ascribed to improved perovskite bulk quality as a result of BHC reducing I_2 to I^-. The steady-state efficiencies of the BHC device and the control (without BHC) are 22.87% and 21.64% (Fig. 5b) at a bias of 0.728 V and 0.710 V respectively. The higher stabilised power output for BHC device agrees well with the *J–V* measurements. Fig. 5c shows the corresponding EQE spectra of the devices. The EQE-integrated J_{SC} over the entire solar spectrum was improved from 30.98 to 31.56 mA cm^{-2} upon the incorporation of BHC, in accordance with the values from *J–V* measurement.

Table 2 Summary of photovoltaic parameters of the champion Pb–Sn PSCs with and without BHC

Conditions	Scan direction	PCE (%)	FF (%)	V_{OC} (V)	J_{SC} (mA cm^{-2})
Control	Reverse	21.86	81.41	0.852	31.53
	Forward	21.34	79.14	0.858	31.43
BHC	Reverse	23.18	83.23	0.875	31.84
	Forward	22.89	82.93	0.864	31.93

This significant enhancement of integrated J_{SC} originates from the notable increase in the spectral response over the 415–600 nm wavelength range. To gain more insights into the reduced non-radiative recombination in BHC devices, we measured the dark *J–V* curves of these devices (Fig. 5d). The dark saturation current density (J_0) of the BHC device was decreased from 3.23 × 10^{-5} mA cm^{-2} (for control device) to 3.94 × 10^{-6} mA cm^{-2}, indicating a reduced leakage current and a smaller barrier for charge transfer. The electrochemical impedance spectroscopy (EIS) results (Fig. 5e) showed increased recombination resistance in BHC incorporated devices, demonstrating the suppression of non-radiative recombination, consistent with the smaller J_0 obtained from the dark *J–V* curve and suppression of I_3^- induced charge trapping. To examine the impact of BHC incorporation on stability, we then conducted MPP tracking to monitor the change of operational stability in ambient air. The encapsulated BHC device maintained 80% of its peak efficiency (*i.e.* T_{S80} lifetime) after continuous 1-sun illumination for 83 h, while the control device showed rapid

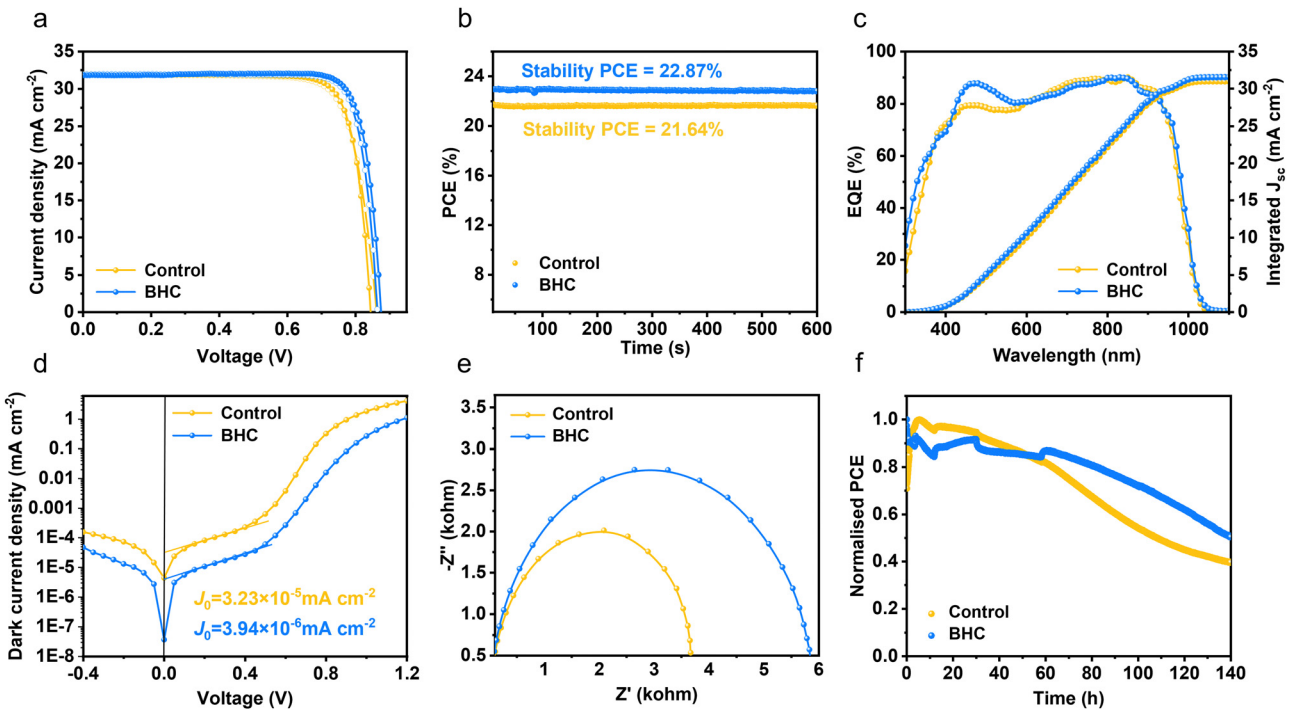

Fig. 5 Device performance and characterisations of Pb–Sn PSCs with and without benzylhydrazine hydrochloride (BHC). (a) *J–V* curves of the champion Pb–Sn PSCs. (b) Steady-state efficiency outputs. (c) Corresponding EQE spectra and integrated J_{SC}. (d) Dark *J–V* curves. (e) Electrochemical impedance spectra (EIS). (f) Continuous MPP tracking of encapsulated devices under a 100 mW cm^{-2} multicolour light emitting diode (LED) solar simulator in ambient air.

degradation (Fig. 5f). We attribute this to the iodine reducing effect of BHC which reduces carrier recombination and improves device efficiency. However, degradation can be observed which indicates that alternate strategies are required, some of which we highlight in Notes S3 and S4, and Fig. S50 and S51 (ESI†). We note that a majority of the testing reported in the literature for Pb–Sn devices utilise a N_2 atmosphere, thereby masking the crucial role of a strong encapsulant and moisture removal for the stability of this technology. We further carried out topographical, structural and optical analysis to identify any changes to the absorber following the addition of BHC (Fig. S50–S52, ESI†). The addition of BHC did not result in a noticeable change to the root mean square roughness of the sample (which was ~49 nm), grain sizes, as well as the crystalline structure nor the optical properties.

Conclusions

In conclusion, we identify that the properties of PEDOT:PSS are significantly modified upon depositing a layer of perovskite owing to undesirable chemical interactions at the interface. More specifically, the nature of these interactions corresponds to the diffusion of the organohalide cations from the perovskite into the underlying PEDOT:PSS layer. This leads to the deactivation of PSS and subsequent de-doping of PEDOT:PSS while simultaneously forming trap states in the perovskite absorber, thereby resulting in device performance loss. The above process further results in the oxidation of I^- to form I_3^-, proceeding first *via* the formation of I_2. The addition of SCN^- reduces the device performance losses by reducing or preventing I_3^- formation. However, when stored under ambient conditions, the reaction of the SCN^- oxidation product $(SCN)_2$ with moisture results in the formation of highly corrosive ICN and HCN, leading to a trade-off between minimising device losses and maintaining ambient stability. We show that I_2 reducing additives can mitigate these losses and improve device efficiency. Using Pb–Sn single junction PSCs, an architecture that to date has heavily relied on the use of PEDOT:PSS as the HTL, we show an improvement in device efficiency upon adding BHC, with a champion efficiency of 23.2% being realised, which is among the highest reported for Pb–Sn mixed PSCs. In parallel, we also observe an improvement of T_{S80} lifetime by ~66% under maximum power point tracking and ambient conditions. Based on our findings, we offer insights for designing next-generation hole extraction materials to enhance efficiency and stability in large-area PSCs.

Experimental

Materials

Formamidinium iodide (FAI, ≥99.99%), methylammonium iodide (MAI, >99.99%) and guanidinium iodide (GAI) were purchased from GreatCell Solar Materials, Australia. Lead(II) iodide (PbI_2, 99.99%) and benzylhydrazine hydrochloride (BHC) were purchased from Tokyo Chemical Industry Co., Ltd (TCI, Japan). Poly(3,4-ethylenedioxythiophene)polystyrene sulfonate (PEDOT:PSS, CLEVIOS™ P VP AI 4083) was purchased from Heraeus, Germany. Poly[(9,9-bis(3′-((*N*,*N*-dimethyl)-*N*-ethyl-ammonium)-propyl)-2,7-fluorene)-*alt*-2,7-(9,9-dioctylfluorene)]dibromide (PFN-Br) was purchased from 1-material, Canada. [4-(3,6-Dimethyl-9*H*-carbazol-9-yl)butyl]phosphonic acid (Me-4PACz) was purchased from Dyenamo, Sweden. Poly(triaryl amine) (PTAA), lead(II) thiocyanate ($Pb(SCN)_2$, 99.5% trace metals basis), guanidine thiocyanate (GASCN, for molecular biology, ≥99%), aluminium oxide (Al_2O_3, 20% (v/v) in 2-propanol), tin(II) iodide (SnI_2, 99.999%), tin(II) fluoride (SnF_2, 99%), ethylenediammonium diiodide ($EDAI_2$, 98%) and ammonium thiocyanate (NH_4SCN), and solvents dimethyl sulfoxide (DMSO, anhydrous, ≥99.9%), *N*,*N*-dimethylformamide (DMF, anhydrous, 99.8%), toluene (anhydrous, 99.8%) and chlorobenzene (CB, 99.9%) were purchased from Sigma Aldrich, UK. Solvents diethyl ether (99.5%, Extra Dry, Acros), methanol (HPLC grade, ≥99.9%), ethanol (anhydrous, >99.5%) and 2-propanol (anhydrous, 99.5%, Acros) were purchased from Fisher Scientific, UK. Caesium iodide (CsI, 99%) was purchased from Alfa Aesar. C_{60} was purchased from Ossila, UK or Nano-C. Bathocuproine (BCP, sublimed grade >99.5%) was purchased from Ossila, UK or Jilin OLED Company, China. Copper (Cu) was purchased from Zhongnuoxincai Co., Ltd.

Substrate cleaning and preparation

ITO coated glass substrates purchased from South China Science and Technology Ltd and from Youxun, China (20 mm × 20 mm with a thickness of 1.1 mm and a sheet resistance of 15 Ω $\square^{-1}$) were first cleaned by sonicating in a 2% (v/v) Hellmanex in water solution for 30 minutes at 35–40 °C. The substrates were then rinsed with deionised water and sonicated in water for a further 30 minutes. Thereafter, they were sequentially cleaned in acetone, 2-propanol and methanol in an ultrasonic bath at ~25 °C for 15 min each and blow dried with N_2. Prior to coating with PEDOT:PSS and PTAA, the substrates were treated with oxygen plasma for 5 min at 200 W using a Diener Zepto system. Prior to coating with Me-4PACz, the substrates were subjected to a UV-O_3 pre-treatment for 10 min using a Jelight UV-O_3 Cleaner Model 24.

For Pb–Sn devices (Sichuan University): the pre-patterned ITO substrates were cleaned by sonicating sequentially in deionised water and anhydrous ethanol for 15 min each, and then dried under N_2 stream and treated by UV-ozone for 15 min.

Solution preparation

PEDOT:PSS: CLEVIOS™ P VP AI 4083 was used as received. Prior to deposition, the dispersion was allowed to warm up to room temperature for 1 hour.

PTAA: a 2 mg mL^{-1} solution of PTAA was prepared in toluene and left to stir overnight inside the glovebox.

Me-4PACz: a 1 mmol L^{-1} solution of Me-4PACz was prepared in ethanol and left to stir overnight inside the glovebox.

PFN-Br: a 0.5 mg mL^{-1} solution of PFN-Br was prepared in methanol and left to stir overnight inside the glovebox.

Al_2O_3: Al_2O_3 20% (v/v) in 2-propanol, obtained from Sigma Aldrich, was diluted in 2-propanol to form a 1 : 1000 Al_2O_3 dispersion.

MAPI: PbI_2 (461 mg) and MAI (159 mg) were weighed into one vial. To this, DMF (595 μL) and DMSO (71 μL) were added and left to stir overnight in the glovebox at room temperature. For MAPI solutions containing $Pb(SCN)_2$ or GASCN, the thiocyanate was weighed into a separate vial and the MAPI solution was added to the powder in the vial and stirred for 1 hour before deposition. For all MAPI solutions, the precursor was stirred at 65 °C for 15 min prior to deposition and maintained at 65 °C during deposition.

PEDOT:PSS with organohalides: MAI, FAI or GAI was added to PEDOT:PSS (filtered through a 0.45 μm PTFE syringe filter) to form dispersions with 1 : 0.25, 1 : 0.5, 1 : 0.75, 1 : 1, 1 : 1.5, 1 : 2, 1 : 3, 1 : 4 and 1 : 5 PSS:organohalide molar ratios.

For Pb–Sn devices: NH_4SCN (2.74 mg), SnF_2 (14.10 mg), CsI (46.77 mg), MAI (85.84 mg), FAI (185.73 mg), SnI_2 (335.27 mg) and PbI_2 (414.91 mg) were dissolved in 1 mL mixed solvent of DMF and DMSO (DMF : DMSO = 3 : 1, v/v) to obtain the $FA_{0.6}MA_{0.3}Cs_{0.1}Pb_{0.5}Sn_{0.5}I_3$ 1.8 M precursor. For the BHC doping precursor, 2.1 mg (0.75 mol%) of BHC was added to 1 mL perovskite precursor. The post-treatment solution was prepared by dissolving 0.5 mg of $EDAI_2$ in 1 mL mixed solvent of toluene and IPA (toluene : IPA= 1 : 1, v/v). For the Pb–Sn devices fabricated at Surrey, 4 mg of GASCN was used instead of NH_4SCN.

Device fabrication

For PEDOT:PSS substrates, PEDOT:PSS was deposited through a 0.45 μm PTFE syringe filter and spun at 5000 rpm for 40 s. The films were then annealed at 150 °C for 30 min. For the PTAA samples, the substrate was coated with 100 μL of the solution, spun at 6000 rpm for 33 s and then annealed at 100 °C for 10 min. For the Me-4PACz substrates, 50 μL of the solution was spread on the substrate and after a waiting time of 5 s, it was spun at 3000 rpm for 30 s. The films were then annealed at 100 °C for 10 min. For the PTAA substrates, PFN-Br was used as a surface compatibiliser, while for the Me-4PACz coated substrates, either PFN-Br or Al_2O_3 nanoparticles was used as previously reported.[15] For the PFN-Br modified samples, 30 μL of the PFN-Br solution was dispensed at 5 s from the spin start time on a substrate spinning at 5000 rpm for 30 s. For Al_2O_3 modified samples, 40 μL of the solution was spin coated at 4000 rpm for 30 s. The perovskite was deposited by spin coating 35 μL of the MAPI at 4000 rpm for 30 s while 600 μL of diethylether, the antisolvent, was dropped at 7 s from the spin start time. The films were annealed, first at 65 °C for 2 min and then at 100 °C for 10 min. C_{60} (20 nm), BCP (7 nm) and Ag (100 nm) were thermally evaporated in an Angstrom EvoVac system.

For the organohalide incorporated PEDOT:PSS samples, the same deposition procedure as PEDOT:PSS was followed using 75 μL of the dispersion.

For Pb–Sn devices (Sichuan University), PEDOT:PSS was spin coated onto the ITO substrate at 4000 rpm for 50 s and annealed at 160 °C for 20 min. Thereafter, the substrates were transferred to the glovebox until they cooled to room temperature. 65 μL of the perovskite precursor was deposited on PEDOT:PSS using the two-step process of 1000 rpm for 10 s and 4000 rpm for 50 s. 600 μL of CB was dropped onto the substrate during the second spin-coating step. Then, the as-prepared perovskite films were annealed for 10 min at 100 °C. For the post-treatment, 100 μL of $EDAI_2$ solution was spin-coated onto the perovskite films at 4000 rpm for 30 s, followed by annealing at 100 °C for 5 min. Then, the substrates were transferred into a vacuum chamber for evaporating 20 nm of C_{60} and 5 nm of BCP at a vacuum pressure of 3×10^{-4} Pa. Finally, 100 nm of Cu was evaporated with a mask.

For the Pb–Sn devices (University of Surrey), PEDOT:PSS was spin coated onto the ITO substrate at 5000 rpm for 40 s and annealed at 150 °C for 30 min in air, and then at 140 °C for 45 min inside the glove box. 50 μL of the perovskite precursor was deposited on PEDOT:PSS using the two-step process of 1000 rpm for 10 s and 4000 rpm for 50 s. 200 μL of CB was dropped onto the substrate during the second spin-coating step. Then, the as-prepared perovskite films were annealed for 10 min at 100 °C. Then, the substrates were transferred into a vacuum chamber for evaporating 20 nm of C_{60} and 7 nm of BCP at a vacuum pressure of less than 4×10^{-4} Pa. Finally, 100 nm of Ag was evaporated with a mask.

Device characterisation

Current (*I*)–voltage (*V*) characteristics of the devices were evaluated using an Enlitech SS-X100R (Class AAA) solar simulator with a Keithley 2450 source measure unit with a scan rate of 0.2 V s^{-1}. The calibration of the simulator was carried out using a KG-5 filtered Si diode. A mask with 0.09 cm^2 aperture area was used to define the active area of the device. All devices were measured without any encapsulation in a N_2 glovebox at a light intensity of 100 mW cm^{-2} (AM 1.5G). The light intensity was calibrated using a silicon reference cell (KG5 filter, Fraunhofer ISE). No preconditioning of the cells was carried out.

For the Pb–Sn devices (Sichuan University): *J*–*V* curves were obtained by using a Keysight Technologies B2901A source meter with a solar simulator (SS-F5, EnliTech) with a scan rate of 0.08 V s^{-1}, dwell time of 100 ms and scan range of −0.1 to 0.9 V under simulated AM 1.5G solar illumination at 100 mW cm^{-2}. The light intensity was calibrated using a silicon reference cell (SRC-00331, EnliTech). The devices were measured using a black shadow mask with an aperture area of 0.0576 cm^2. No preconditioning of the cells was carried out.

For the Pb–Sn devices (University of Surrey): *J*–*V* curves were obtained by using a Keysight Technologies B2901A source meter with a solar simulator (SS-F5, EnliTech) with a scan rate of 0.08 V s^{-1}, dwell time of 100 ms and scan range of −0.1 to 1 V under simulated AM 1.5G solar illumination at 100 mW cm^{-2}. The light intensity was calibrated using a silicon reference cell (Newport). The devices were measured using a shadow mask with an aperture area of 0.09 cm^2. Measurements were carried out under ambient conditions without any encapsulation at a temperature of ~25 °C and a relative humidity of 30–35%. No preconditioning of the cells was carried out.

EQE measurements of the MAPI devices were carried out using a Bentham PVE300 system. All measurements were carried out under ambient conditions. Reflectance measurements were carried out using an integrating sphere incorporated into the

same system. For the Pb–Sn devices, EQE measurements were taken with an Enlitech QE-R system. All devices were measured without any encapsulation under ambient conditions at a temperature of ~25 °C and a relative humidity of 30–35%.

TPC and IMPS measurements were conducted using Fluxim's PAIOS all-in-one test setup with a pixel area of 4.5 mm^2.

EIS was measured using CHI600E. The Nyquist plots of the EIS were obtained in the frequency range of 1 MHz to 1 Hz with a bias voltage of 0.8 V and amplitude of 5 mV.

Stability testing: no encapsulation was used for the stability testing. For ISOS-D-1 testing, the samples were stored in the dark under ambient conditions with a relative humidity of ~65%. For ISOS-D1I testing, the samples were stored in the dark in a N_2 glove box.

For the Pb–Sn devices: MPP tracking was performed with a multicolour LED solar simulator (Guangzhou Crysco Equipment Co. Ltd) under AM 1.5G, 100 mW cm^{-2}.

Thin film characterisation

SEM images were acquired using a TESCAN MIRA2 SEM under an accelerating voltage of 5 kV or a ThermoFischer Scientific Apreo under an accelerating voltage of 2 kV. Grain size analysis was carried out using ImageJ software.

GIXRD measurements were taken using a Panalytical X'pert Pro diffractometer using a GI stage with a Cu Kα1 X-ray source driven at 40 kV.

XPS spectra were obtained on a Thermo Fisher Scientific Instruments K-Alpha+ spectrometer consisting of a monochromated Al Kα X-ray source ($h\nu$ = 1486.6 eV) with a spot size of ~400 μm radius. A pass energy of 200 eV was used for acquisition of the survey spectra. For obtaining high resolution core level spectra, a pass energy of 50 eV was used for all elements. For correction of possible charging effects that can occur during acquisition, the obtained spectra were charge referenced against the C 1s peak (285 eV). Fitting of the spectra was carried out using the manufacturers' Avantage software.

UPS was taken on a Thermo Scientific Theta Probe system using He–I excitation (21.22 eV). A −9 V bias was applied during measurement to the samples prepared on ITO substrates. The binding energy scale was calibrated to the Fermi edge of clean Au at 0 eV.

For TAS measurements, all samples were given glass-lid encapsulation. The output of a Ti:sapphire amplifier system (Spectra Physics Solstice Ace) operating at 1 kHz and generating ~100 fs pulses was used as a femtosecond laser source. For measurements, a 400 nm pump with fluence of ~2.3 μJ cm^{-2} (incident from the perovskite layer), corresponding to an injected carrier density of 1.06×10^{17} cm^{-3} was used. The 400 nm pump pulses were created by sending the 800-nm fundamental beam of the Solstice Ace through a second harmonic generating (SHG) beta barium borate (BBO) crystal of 1 mm thickness (Eksma Optics). The pump was blocked by a chopper wheel rotating at 500 Hz. The broadband white light was provided by the Disco (Leukos Laser, STM-2-UV) and the pump–probe decay was controlled electronically. The white light was split into two identical beams (probe and reference) by a 50/50 beamsplitter. The reference beam passing through the sample did not interact with the pump, which allows for correcting for any shot-to-shot fluctuations in the probe that would otherwise greatly increase the structured noise in the experiments. Based on this arrangement, small signals with $\Delta T/T \sim 10^{-5}$ could be measured. The transmitted probe and reference pulses were collected with a silicon dual-line array detector (Hamamatsu S8381-1024Q, spectrograph: Andor Shamrock SR-303i-B) driven and read out by a custom-built board (Stresing Entwicklungsbüro). The recombination rate constants were calculated by fitting the decay characteristics using the general recombination rate equation:[52]

$$-\frac{dn}{dt} = k_1 n + k_2 n^2 + k_3 n^3$$

where k_1 is the Shockley–Read–Hall monomolecular recombination rate (corresponding to traps), k_2 is the radiative bimolecular recombination rate, and k_3 is the Auger recombination rate. In this study, we focus on the low carrier density region where k_1 dominates the recombination process and extract the k_1 rate constant.

ToF-SIMS (NREL): an ION-TOF ToF-SIMS V spectrometer was utilised for depth profiling using methods covered in detail in previous reports.[53] Analysis was completed utilising a 3-lens 30 keV BiMn primary ion gun. High mass resolution depth profiles were completed with a 30 keV Bi_3^+ primary ion beam (0.8 pA pulsed beam current), and a 50 × 50 μm area was analysed with a 128 : 128 primary beam raster. Sputter depth profiling was accomplished with a 600 eV Cesium ion beam (2.6 nA sputter current) with a raster of 150 × 150 μm^2.

ToF-SIMS chemical depth profiling (NPL): samples were prepared following the configuration of glass/ITO/PEDOT:PSS/MAPI (with or without SCN^- additives)/polymethylmethacrylate (PMMA)/Gorilla 2-part epoxy (5 min)/glass. The glass/ITO used was 15 mm × 15 mm while cover glass slips cut to the dimensions of 25 mm × 25 mm were used on the top. PMMA 950k A6 from Microchem was coated on the perovskite to realise a 200 nm thick film (inside a N_2 glove box) and was left to cure overnight. The Gorilla epoxy was then carefully coated onto the samples and the glass cover slips were carefully placed on top and left to cure for at least 24 hours inside a N_2 glove box. The samples were then subjected to impact by dropping from ~1 m. 3D chemical depth profiling of the cleaved samples near the PEDOT:PSS/perovskite interface was carried out using a Hybrid ToF-SIMS / OrbiSIMS (Hybrid SIMS) instrument from IONTOF GmbH. The ToF-SIMS data were acquired in positive ion polarity mode in dual-beam mode by raster scanning a 30 keV Bi_3^+ primary ion beam (delivering 0.21 pA at a cycle time of 200 μs) of 200 × 200 μm^2 at the centre of a 300 × 300 μm^2 sputter crater formed using a 2 keV O_2 beam. The O_2 beam delivered a current of 1.02 nA. The analysis was performed in the "non-interlaced" mode with a low-energy (20 eV) electron flood gun employed to neutralise charge build up.

UV-vis spectra of the PEDOT:PSS + organohalide thin films were acquired using a Cary 5000 spectrophotometer, while the UV-vis spectra of the PEDOT:PSS dispersions incorporating organohalides were obtained using a Shimadzu 2600 spectrophotometer with an integrating sphere accessory.

EPR spectroscopy was collected on a Bruker Magnettech ESR 5000 at a temperature of 29 °C, averaged over 3 sweeps using a microwave power of 4 MW.

^{1}H and ^{13}C NMR were collected on a Bruker 400 MHz NMR spectrometer using $CDCl_3$ as a deuterated solvent. Data were collected using top spin data acquisition software. Data chemical shifts were corrected to the 7.26 ppm peak of $CDCl_3$ using Mestrenova software.

Attenuated total reflectance Fourier transform infrared spectroscopy (ATR-FTIR) was carried out using a Carey 630 FTIR benchtop spectrometer using a Diamond ATR configuration with a KBr window.

MS measurements were acquired by direct injection using an atmospheric pressure chemical ionisation (APCI) ion source connected to a Thermo Fisher Q-Exactive Orbitrap mass spectrometer using a capillary temperature of 320 °C and the discharge voltage was set between 3.5 and 4.0 kV. The mass spectrometer was operated in positive and negative ionisation mode.

Cyclic voltammetry was carried out using an electrolyte of 0.15 M *n*-butylammonium hexafluorophosphate in 50 mL anhydrous acetonitrile (99.8+%), dried over molecular sieves. CV data were collected on a Gamry 1010E potentiostat using a $AgNO_3$ reference electrode (connected through a ceramic luggin capillary), Pt counter and Pt working electrode (2 mm diameter). The samples were measured at a scan rate of 100 mV s^{-1}. To the electrolyte solution, 2 mM of the sample was dissolved before the solution was degassed in N_2. In experiments where –SCN was added to I_2 or *vice versa*, 2 scan cycles were collected before the secondary compound was added, degassed, and remeasured.

Optical images of PEDOT:PSS incorporating organohalides were obtained using a Keyence VHX-5000 digital microscope.

DFT and TD-DFT calculations were processed using Gaussian 16 Software. For each calculation the geometry was optimised using a hybrid 6-311G(d,p) [H,C,N,O,S], LANL2DZ [I] basis set and either unrestricted B3LYP or ωB97XD functionals with a Grimme's dispersion correction modifier (GD3).

Calculation of the oscillator strength of the PEDOT 12-monomer chain: to calculate the oscillator strength of the PEDOT under different oxidation states, first the PEDOT geometry was optimised at between 0 and 50% oxidation (PEDOT0–PEDOT6) using uB3LYP with Grimme's D2 dispersion or uωB97XD functionals. From the calculated ground state geometries, the energies for different spin multiplicities were calculated allowing for the lowest energy spin multiplicity to be determined. From this lowest energy predicted spin multiplicity, TD-DFT was used to predict electronic transitions and give a prediction of the oscillator strength across visible wavelengths.

Calculation of binding/dissociation/reaction free energies: to calculate the gas-phase ion binding energies, the molecular geometries were first optimised before performing frequency calculations to obtain the zero-point energy corrected free energies at a default temperature of 298.15 K.

$$\Delta G_g^0 = \Delta G_g(\text{PEDOT:I}_3) + \Delta G_g(\text{A:PSS}) - [\Delta G_g(\text{PEDOT:PSS}) + \Delta G_g(\text{A:I}_3)]$$

For this work, only gas phase calculations were performed owing to the inability of SMD models to accurately describe the hydration environment within PSS micelles. This is particularly important owing to the effects of polar mediums to screen the ionic charges. The predicted thermodynamic quantities were calculated using the equations below. In this work, a PSS monomer was used with a PEDOT trimer $PEDOT_3^{+1}$:

$$4\text{PSSH} + 4\text{AI} + \text{O}_2 \rightarrow 4\text{PSS}^-\text{MA}^+ + 2\text{H}_2\text{O} + 2\text{I}_2$$

$$\Delta G_r = (1/4)[4\Delta G(\text{A:SS}_1) + 2\Delta G(\text{H}_2\text{O}) + 2\Delta G(\text{I}_2) - [4\Delta G(\text{SS}_1\text{H}) + \Delta G(\text{O}_2) + 4\Delta G(\text{AI})]]$$

$$\Delta G_b(\text{PSS:A}) = [\Delta G(\text{PSS:A}) - [\Delta G(\text{PSS}_1) + \Delta G(\text{A})]]$$

$$G_d(\text{PSS:PEDOT/A}) = [\Delta G(\text{SS}_1\text{:A}) + \Delta G(\text{PEDOT}_3^{+1}) - [\Delta G(\text{PEDOT:SS}_1) + \Delta G(\text{A}^{+1})]]$$

$$\Delta G_b(\text{A:I}) = [\Delta G(\text{A:I}) - [\Delta G(\text{A}^+) + \Delta G(\text{I}^-)]]$$

Author contributions

Conceptualisation: W. H. K. P., T. W., K. D. G. I. J., S. A. H., S. R. P. S. Methodology: W. H. K. P., T. W., Y. X., D. W. Z., K. D. G. I. J., S. A. H., S. R. P. S. Investigation: W. H. K. P., T. W., Y. X., J. Z., Y. Zhou, G. F. T., M. G. M., S. P. H., S. J., L. D., S. S., T. J. M., S. J. H., Y. Zhao, K. D. G. I. J. Funding acquisition: S. P. H., S. J., T. J. M., Y. Zhao, S. D. S., D. W. Z., W. Z., K. D. G. I. J., S. A. H., S. R. P. S. Supervision: T. J. M., S. D. S., G. F. T., D. W. Z., W. Z., K. D. G. I. J., S. A. H., S. R. P. S. Writing – original draft: W. H. K. P., T. W.,Y. X., K. D. G. I. J., S. A. H., S. R. P. S. Writing – review & editing: W. H. K. P., T. W., Y. X., J. Z., Y. Zhou, G. F. T., M. G. M., S. P. H., S. J., L. D., S. S., T. J. M., S. J. H., Y. Zhao, S. D. S., D. W. Z., W. Z., K. D. G. I. J., S. A. H., S. R. P. S.

Data availability

Data for this article are available at the University of Surrey Open Research Repository at **https://openresearch.surrey.ac.uk/esploro/**.

Conflicts of interest

S. D. S. is a co-founder of Swift Solar Inc. S. J. is an employee at Fluxim AG.

Acknowledgements

S. R. P. S. and W. Z. acknowledge support from the Engineering and Physical Sciences Research Council (EPSRC) Reference EP/V027131/1. S. R. P. S. and S. J. gratefully acknowledge funding through the MUSICODE project (Grant ID: 953187) from the European Union's Horizon 2020. S. R. P. S. and K. D. G. I. J. acknowledge funding from the Equality Foundation of Hong Kong. W. H. K. P. gratefully acknowledges funding from the University of Surrey Doctoral College through the DCSA4

scheme. K. D. G. I. J. acknowledges support from the Royal Society of Chemistry, UK (Grant ID: RGS\R1\211403). S. A. H. gratefully acknowledges funding from the Engineering and Physical Sciences Research Council (EPSRC, EP/X012344/1). T. W. gratefully acknowledges funding from the Engineering and Physical Sciences Research Council Doctoral Training Partnership (EPSRC DTP, EP/T51780X/1). S. D. S. and L. D. acknowledge funding support from the European Research Council under the European Union's Horizon 2020 research and innovation programme (ERC fundings: PEROVSCI, 957513 & HYPERION, 756962). S. D. S. acknowledges support from the Royal Society and Tata Group (UF150033). T. J. M. thanks the Royal Commission for the Exhibition of 1851 for their financial support through a Research Fellowship. T. J. M. also acknowledges funding from a Royal Society University Research Fellowship (URF/R1/221834) and the Royal Society Research Fellows Enhanced Research Expenses (RF/ERE/221066). D. W. Z. acknowledges financial support from the National Natural Science Foundation of China (No. 62174112). Y. Zhao, G. F. T. and Y. Zhou acknowledge support and funding from the UK Government's Department for Science, Innovation and Technology (DSIT) through the UK's National Measurement System (NMS) programme. The authors thank Dr Rachel C. Kilbride (University of Sheffield, UK) and Dr Joel A. Smith (University of Oxford, UK) for useful discussions on GIXRD analysis. The authors also thank Ms Lauren Tidmarsh for assistance with the deposition of gold for cross-sectional imaging and SEM imaging of lead–tin perovskites. This work was authored in part by the National Renewable Energy Laboratory, operated by Alliance for Sustainable Energy, LLC, for the U.S. Department of Energy (DOE) under Contract No. DE-AC36-08GO28308. Funding provided by the U.S. Department of Energy Office of Energy Efficiency and Renewable Energy Solar Energy Technologies Office Agreement #38256, Advanced Perovskite Solar Cells and Modules. The views expressed in the article do not necessarily represent the views of the DOE or the U.S. Government. The U.S. Government retains and the publisher, by accepting the article for publication, acknowledges that the U.S. Government retains a nonexclusive, paid-up, irrevocable, worldwide license to publish or reproduce the published form of this work, or allow others to do so, for U.S. Government purposes.

Notes and references

1 M. A. Green, E. D. Dunlop, M. Yoshita, N. Kopidakis, K. Bothe, G. Siefer, D. Hinken, M. Rauer, J. Hohl-Ebinger and X. Hao, *Prog. Photovoltaics Res. Appl.*, 2024, **32**, 425–441.

2 S. Hu, K. Otsuka, R. Murdey, T. Nakamura, M. A. Truong, T. Yamada, T. Handa, K. Matsuda, K. Nakano, A. Sato, K. Marumoto, K. Tajima, Y. Kanemitsu and A. Wakamiya, *Energy Environ. Sci.*, 2022, **15**, 2096–2107.

3 J. Suo, B. Yang, E. Mosconi, D. Bogachuk, T. A. S. Doherty, K. Frohna, D. J. Kubicki, F. Fu, Y. Kim, O. Er-Raji, T. Zhang, L. Baldinelli, L. Wagner, A. N. Tiwari, F. Gao, A. Hinsch, S. D. Stranks, F. De Angelis and A. Hagfeldt, *Nat. Energy*, 2024, **9**, 172–183.

4 H. Zhu, S. Teale, M. N. Lintangpradipto, S. Mahesh, B. Chen, M. D. McGehee, E. H. Sargent and O. M. Bakr, *Nat. Rev. Mater*, 2023, **8**, 569–586.

5 R. Azmi, E. Ugur, A. Seitkhan, F. Aljamaan, A. S. Subbiah, J. Liu, G. T. Harrison, M. I. Nugraha, M. K. Eswaran, M. Babics, Y. Chen, F. Xu, T. G. Allen, A. ur Rehman, C.-L. Wang, T. D. Anthopoulos, U. Schwingenschlögl, M. De Bastiani, E. Aydin and S. De Wolf, *Science*, 2022, **376**, 73–77.

6 S. M. Park, M. Wei, J. Xu, H. R. Atapattu, F. T. Eickemeyer, K. Darabi, L. Grater, Y. Yang, C. Liu, S. Teale, B. Chen, H. Chen, T. Wang, L. Zeng, A. Maxwell, Z. Wang, K. R. Rao, Z. Cai, S. M. Zakeeruddin, J. T. Pham, C. M. Risko, A. Amassian, M. G. Kanatzidis, K. R. Graham, M. Grätzel and E. H. Sargent, *Science*, 2023, **381**, 209–215.

7 X. Liu, D. Luo, Z.-H. Lu, J. S. Yun, M. Saliba, S. Il Seok and W. Zhang, *Nat. Rev. Chem.*, 2023, **7**, 462–479.

8 M. Wang, Z. Shi, C. Fei, Z. J. D. Deng, G. Yang, S. P. Dunfield, D. P. Fenning and J. Huang, *Nat. Energy*, 2023, **8**, 1229–1239.

9 T. Webb and S. A. Haque, *Energy Environ. Sci.*, 2024, **17**, 3244–3269.

10 C. C. Boyd, R. C. Shallcross, T. Moot, R. Kerner, L. Bertoluzzi, A. Onno, S. Kavadiya, C. Chosy, E. J. Wolf, J. Werner, J. A. Raiford, C. de Paula, A. F. Palmstrom, Z. J. Yu, J. J. Berry, S. F. Bent, Z. C. Holman, J. M. Luther, E. L. Ratcliff, N. R. Armstrong and M. D. McGehee, *Joule*, 2020, **4**, 1759–1775.

11 Y. Liu, B. Ding, G. Zhang, X. Ma, Y. Wang, X. Zhang, L. Zeng, M. K. Nazeeruddin, G. Yang and B. Chen, *Adv. Sci.*, 2024, **11**, 2309111.

12 X. Fan, N. E. Stott, J. Zeng, Y. Li, J. Ouyang, L. Chu and W. Song, *J. Mater. Chem. A*, 2023, **11**, 18561–18591.

13 S. Liu, J. Li, W. Xiao, R. Chen, Z. Sun, Y. Zhang, X. Lei, S. Hu, M. Kober-Czerny, J. Wang, F. Ren, Q. Zhou, H. Raza, Y. Gao, Y. Ji, S. Li, H. Li, L. Qiu, W. Huang, Y. Zhao, B. Xu, Z. Liu, H. J. Snaith, N.-G. Park and W. Chen, *Nature*, 2024, **632**, 536–542.

14 L. Wagner, J. Suo, B. Yang, D. Bogachuk, E. Gervais, R. Pietzcker, A. Gassmann and J. C. Goldschmidt, *Joule*, 2024, **8**, 1142–1160.

15 W. H. K. Perera, M. G. Masteghin, H. Shim, J. D. Davies, J. L. Ryan, S. J. Hinder, J. S. Yun, W. Zhang, K. D. G. I. Jayawardena and S. R. P. Silva, *Sol. RRL*, 2023, **7**, 2300388.

16 M. Stolterfoht, C. M. Wolff, J. A. Márquez, S. Zhang, C. J. Hages, D. Rothhardt, S. Albrecht, P. L. Burn, P. Meredith, T. Unold and D. Neher, *Nat. Energy*, 2018, **3**, 847–854.

17 S.-C. Liu, H.-Y. Lin, S.-E. Hsu, D.-T. Wu, S. Sathasivam, M. Daboczi, H.-J. Hsieh, C.-S. Zeng, T.-G. Hsu, S. Eslava, T. J. Macdonald and C.-T. Lin, *J. Mater. Chem. A*, 2024, **12**, 2856–2866.

18 J. Chen, J. Luo, E. Hou, P. Song, Y. Li, C. Sun, W. Feng, S. Cheng, H. Zhang, L. Xie, C. Tian and Z. Wei, *Nat. Photonics*, 2024, **18**, 464–470.

19 C.-H. Kuan, Y.-C. Chen, S. Narra, C.-F. Chang, Y.-W. Tsai, J.-M. Lin, G.-R. Chen and E. W.-G. Diau, *ACS Energy Lett.*, 2024, **9**, 2351–2357.

20 G. Kapil, T. Bessho, T. Maekawa, A. K. Baranwal, Y. Zhang, M. A. Kamarudin, D. Hirotani, Q. Shen, H. Segawa and S. Hayase, *Adv. Energy Mater.*, 2021, **11**, 2101069.
21 R. Lin, Y. Wang, Q. Lu, B. Tang, J. Li, H. Gao, Y. Gao, H. Li, C. Ding, J. Wen, P. Wu, C. Liu, S. Zhao, K. Xiao, Z. Liu, C. Ma, Y. Deng, L. Li, F. Fan and H. Tan, *Nature*, 2023, **620**, 994–1000.
22 Z. Wang, L. Zeng, T. Zhu, H. Chen, B. Chen, D. J. Kubicki, A. Balvanz, C. Li, A. Maxwell, E. Ugur, R. dos Reis, M. Cheng, G. Yang, B. Subedi, D. Luo, J. Hu, J. Wang, S. Teale, S. Mahesh, S. Wang, S. Hu, E. D. Jung, M. Wei, S. M. Park, L. Grater, E. Aydin, Z. Song, N. J. Podraza, Z.-H. Lu, J. Huang, V. P. Dravid, S. De Wolf, Y. Yan, M. Grätzel, M. G. Kanatzidis and E. H. Sargent, *Nature*, 2023, **618**, 74–79.
23 R. He, W. Wang, Z. Yi, F. Lang, C. Chen, J. Luo, J. Zhu, J. Thiesbrummel, S. Shah, K. Wei, Y. Luo, C. Wang, H. Lai, H. Huang, J. Zhou, B. Zou, X. Yin, S. Ren, X. Hao, L. Wu, J. Zhang, J. Zhang, M. Stolterfoht, F. Fu, W. Tang and D. Zhao, *Nature*, 2023, **618**, 80–86.
24 D. Di Girolamo, E. Aktas, C. Ponti, J. Pascual, G. Li, M. Li, G. Nasti, F. Alharthi, F. Mura and A. Abate, *Mater. Adv.*, 2022, **3**, 9083–9089.
25 L. V. Kayser and D. J. Lipomi, *Adv. Mater.*, 2019, **31**, 1806133.
26 J. Zhu, Y. Xu, Y. Luo, J. Luo, R. He, C. Wang, Y. Wang, K. Wei, Z. Yi, Z. Gao, J. Wang, J. You, Z. Zhang, H. Lai, S. Ren, X. Liu, C. Xiao, C. Chen, J. Zhang, F. Fu and D. Zhao, *Sci. Adv.*, 2024, **10**, eadl2063.
27 Y.-C. Chin, M. Daboczi, C. Henderson, J. Luke and J.-S. Kim, *ACS Energy Lett.*, 2022, **7**, 560–568.
28 D.-T. Wu, W.-X. Zhu, Y. Dong, M. Daboczi, G. Ham, H.-J. Hsieh, C.-J. Huang, W. Xu, C. Henderson, J.-S. Kim, S. Eslava, H. Cha, T. J. Macdonald and C.-T. Lin, *Small Methods*, 2024, 2400302.
29 H. Jin, M. D. Farrar, J. M. Ball, A. Dasgupta, P. Caprioglio, S. Narayanan, R. D. J. Oliver, F. M. Rombach, B. W. J. Putland, M. B. Johnston and H. J. Snaith, *Adv. Funct. Mater.*, 2023, **33**, 2303012.
30 L. Lanzetta, T. Webb, N. Zibouche, X. Liang, D. Ding, G. Min, R. J. E. Westbrook, B. Gaggio, T. J. Macdonald, M. S. Islam and S. A. Haque, *Nat. Commun.*, 2021, **12**, 2853.
31 S. Chen, X. Xiao, H. Gu and J. Huang, *Sci. Adv.*, 2024, **7**, eabe8130.
32 Z. Liang, Y. Zhang, H. Xu, W. Chen, B. Liu, J. Zhang, H. Zhang, Z. Wang, D.-H. Kang, J. Zeng, X. Gao, Q. Wang, H. Hu, H. Zhou, X. Cai, X. Tian, P. Reiss, B. Xu, T. Kirchartz, Z. Xiao, S. Dai, N.-G. Park, J. Ye and X. Pan, *Nature*, 2023, **624**, 557–563.
33 M. Saliba, T. Matsui, K. Domanski, J.-Y. Seo, A. Ummadisingu, S. M. Zakeeruddin, J.-P. Correa-Baena, W. R. Tress, A. Abate, A. Hagfeldt and M. Grätzel, *Science*, 2016, **354**, 206–209.
34 J. Tong, Q. Jiang, A. J. Ferguson, A. F. Palmstrom, X. Wang, J. Hao, S. P. Dunfield, A. E. Louks, S. P. Harvey, C. Li, H. Lu, R. M. France, S. A. Johnson, F. Zhang, M. Yang, J. F. Geisz, M. D. McGehee, M. C. Beard, Y. Yan, D. Kuciauskas, J. J. Berry and K. Zhu, *Nat. Energy*, 2022, **7**, 642–651.
35 S. Martani, Y. Zhou, I. Poli, E. Aktas, D. Meggiolaro, J. Jiménez-López, E. L. Wong, L. Gregori, M. Prato, D. Di Girolamo, A. Abate, F. De Angelis and A. Petrozza, *ACS Energy Lett.*, 2023, **8**, 2801–2808.
36 J.-J. Cao, Y.-H. Lou, W.-F. Yang, K.-L. Wang, Z.-H. Su, J. Chen, C.-H. Chen, C. Dong, X.-Y. Gao and Z.-K. Wang, *Chem. Eng. J.*, 2022, **433**, 133832.
37 J. Werner, T. Moot, T. A. Gossett, I. E. Gould, A. F. Palmstrom, E. J. Wolf, C. C. Boyd, M. F. A. M. van Hest, J. M. Luther, J. J. Berry and M. D. McGehee, *ACS Energy Lett.*, 2020, **5**, 1215–1223.
38 C. Kamaraki, M. T. Klug, V. J. Y. Lim, N. Zibouche, L. M. Herz, M. S. Islam, C. Case and L. Miranda Perez, *Adv. Energy Mater.*, 2024, **14**, 2302916.
39 M. V. Khenkin, E. A. Katz, A. Abate, G. Bardizza, J. J. Berry, C. Brabec, F. Brunetti, V. Bulović, Q. Burlingame, A. Di Carlo, R. Cheacharoen, Y. B. Cheng, A. Colsmann, S. Cros, K. Domanski, M. Dusza, C. J. Fell, S. R. Forrest, Y. Galagan, D. Di Girolamo, M. Grätzel, A. Hagfeldt, E. von Hauff, H. Hoppe, J. Kettle, H. Köbler, M. S. Leite, S. (Frank) Liu, Y. L. Loo, J. M. Luther, C. Q. Ma, M. Madsen, M. Manceau, M. Matheron, M. McGehee, R. Meitzner, M. K. Nazeeruddin, A. F. Nogueira, Ç. Odabaşı, A. Osherov, N. G. Park, M. O. Reese, F. De Rossi, M. Saliba, U. S. Schubert, H. J. Snaith, S. D. Stranks, W. Tress, P. A. Troshin, V. Turkovic, S. Veenstra, I. Visoly-Fisher, A. Walsh, T. Watson, H. Xie, R. Yıldırım, S. M. Zakeeruddin, K. Zhu and M. Lira-Cantu, *Nat. Energy*, 2020, **5**, 35–49.
40 M. M. de Kok, M. Buechel, S. I. E. Vulto, P. van de Weijer, E. A. Meulenkamp, S. H. P. M. de Winter, A. J. G. Mank, H. J. M. Vorstenbosch, C. H. L. Weijtens and V. van Elsbergen, *Phys. Status Solidi*, 2004, **201**, 1342–1359.
41 H. Park, S. H. Lee, F. S. Kim, H. H. Choi, I. W. Cheong and J. H. Kim, *J. Mater. Chem. A*, 2014, **2**, 6532–6539.
42 V. Gueskine, A. Singh, M. Vagin, X. Crispin and I. Zozoulenko, *J. Phys. Chem. C*, 2020, **124**, 13263–13272.
43 A. de Izarra, C. Choi, Y. H. Jang and Y. Lansac, *J. Phys. Chem. B*, 2021, **125**, 1916–1923.
44 C. Choi, A. de Izarra, I. Han, W. Jeon, Y. Lansac and Y. H. Jang, *J. Phys. Chem. B*, 2022, **126**, 1615–1624.
45 J. L. Gazquez and F. Mendez, *J. Phys. Chem.*, 1994, **98**, 4591–4593.
46 V. A. Kokorekin, S. V. Neverov, V. N. Kuzina and V. A. Petrosyan, *Molecules*, 2020, **25**, 4169.
47 V. A. Kokorekin, V. L. Sigacheva and V. A. Petrosyan, *Tetrahedron Lett.*, 2014, **55**, 4306–4309.
48 V. A. Kokorekin, R. R. Yaubasarova, S. V. Neverov and V. A. Petrosyan, *Eur. J. Org. Chem.*, 2019, 4233–4238.
49 G. A. Bowmaker and D. A. Rogers, *J. Chem. Soc., Dalton Trans.*, 1981, 1146–1151.
50 S. Bitton and N. Tessler, *Energy Environ. Sci.*, 2023, **16**, 2621–2628.
51 L. A. Frolova, S. Y. Luchkin, Y. Lekina, L. G. Gutsev, S. A. Tsarev, I. S. Zhidkov, E. Z. Kurmaev, Z. X. Shen, K. J. Stevenson, S. M. Aldoshin and P. A. Troshin, *Adv. Energy Mater.*, 2021, **11**, 2002934.
52 D. W. deQuilettes, K. Frohna, D. Emin, T. Kirchartz, V. Bulovic, D. S. Ginger and S. D. Stranks, *Chem. Rev.*, 2019, **119**, 11007–11019.
53 S. P. Harvey, J. Messinger, K. Zhu, J. M. Luther and J. J. Berry, *Adv. Energy Mater.*, 2020, **10**, 1903674.